

MIT Open Access Articles

Triply Loaded Nitroxide Brush-Arm Star Polymers Enable Metal-Free Millimetric Tumor Detection by Magnetic Resonance Imaging

The MIT Faculty has made this article openly available. **Please share** how this access benefits you. Your story matters.

Citation: Nguyen, Hung V.-T. "Triply Loaded Nitroxide Brush-Arm Star Polymers Enable Metal-Free Millimetric Tumor Detection by Magnetic Resonance Imaging." ACS Nano, 12, 11, (November 2018): 11343-11354 © 2018 American Chemical Society

As Published: <https://doi.org/10.1021/acsnano.8b06160>

Publisher: American Chemical Society

Persistent URL: <https://hdl.handle.net/1721.1/123532>

Version: Author's final manuscript: final author's manuscript post peer review, without publisher's formatting or copy editing

Terms of Use: Article is made available in accordance with the publisher's policy and may be subject to US copyright law. Please refer to the publisher's site for terms of use.





Published in final edited form as:

ACS Nano. 2018 November 27; 12(11): 11343–11354. doi:10.1021/acsnano.8b06160.

Triply Loaded Nitroxide Brush-Arm Star Polymers Enable Metal-Free Millimetric Tumor Detection by Magnetic Resonance Imaging

Hung V.-T. Nguyen^{#†,∇,○}, Alexandre Detappe^{#,‡,∇,○}, Nolan M. Gallagher[†], Hui Zhang[◆], Peter Harvey[‡], Changcun Yan[◆], Clelia Mathieu[∇], Matthew R. Golder[†], Yivan Jiang[†], Maria Francesca Ottaviani[#], Alan Jasanoff^{‡,§,||}, Andrzej Rajca[◆], Irene Ghobrial^{∇,○}, P. Peter Ghoroghchian^{*,‡,∇,○}, and Jeremiah A. Johnson^{*,†,‡}

[†]Department of Chemistry, Massachusetts Institute of Technology, 77 Massachusetts Avenue, Cambridge, Massachusetts 02139, United States

[‡]Department of Biological Engineering, Massachusetts Institute of Technology, 77 Massachusetts Avenue, Cambridge, Massachusetts 02139, United States

[§]Department of Brain and Cognitive Sciences, Massachusetts Institute of Technology, 77 Massachusetts Avenue, Cambridge, Massachusetts 02139, United States

^{||}Department of Nuclear Science and Engineering Massachusetts Institute of Technology, 77 Massachusetts Avenue, Cambridge, Massachusetts 02139, United States

[‡]David H. Koch Institute for Integrative Cancer Research, Massachusetts Institute of Technology, 77 Massachusetts Avenue, Cambridge, Massachusetts 02139, United States

[#]Department of Pure and Applied Sciences, University of Urbino, Urbino 61029, Italy

[∇]Department of Medical Oncology, Dana-Farber Cancer Institute, 450 Brookline Avenue, Boston, Massachusetts 02215, United States

[○]Harvard Medical School, 25 Shattuck Street, Boston, Massachusetts 02115, United States

[◆]Department of Chemistry, University of Nebraska, Lincoln, Nebraska 68588, United States

^{*} These authors contributed equally to this work.

Abstract

Nitroxides occupy a privileged position among plausible metal-free magnetic resonance imaging (MRI) contrast agents (CAs) due to their inherently low-toxicity profiles; nevertheless, their translational development has been hindered by a lack of appropriate contrast sensitivity. Nanostructured materials with high nitroxide densities, where each individual nitroxide within a macromolecular construct contributes to the image contrast, could address this limitation, but the synthesis of such materials remains challenging. Here, we report a modular and scalable synthetic

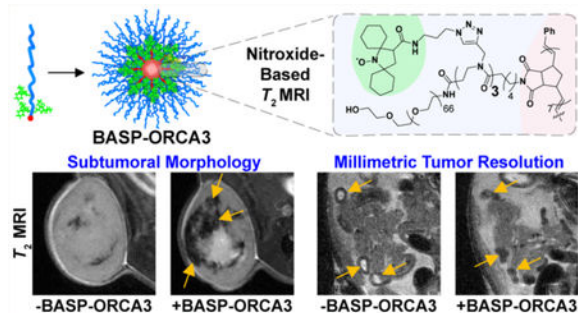
*Corresponding Authors ppg@mit.edu., jaj2109@mit.edu.
Author Contributions

Notes

The authors declare no competing financial interest.

approach to nitroxide-based brush-arm star polymer (BASP) organic radical CAs (ORCAs) with high nitroxide loadings. The optimized ~30 nm diameter “BASP-ORCA3” displays outstanding T_2 sensitivity with a very high molecular transverse relaxivity ($r_2 > 1000 \text{ mM}^{-1} \text{ s}^{-1}$). BASP-ORCA3 further exhibits excellent stability *in vivo*, no acute toxicity, and highly desirable pharmacokinetic and biodistribution profiles for longitudinal detection of tumors by MRI. When injected intravenously into mice bearing subcutaneous plasmacytomas, BASP-ORCA3 affords distinct *in vivo* visualization of tumors on translationally relevant time scales. Leveraging its high sensitivity, BASP-ORCA3 enables efficient mapping of tumor necrosis, which is an important biomarker to predict therapeutic outcomes. Moreover, BASP-ORCA3 allows for detection of millimetric tumor implants in a disseminated murine model of advanced-stage human ovarian cancer that possess genetic, histological, and vascular characteristics that are similar to those seen in patients. This work establishes BASP-ORCA3 as a promising metal-free spin contrast agent for MRI.

Graphical Abstract



Keywords

magnetic resonance imaging; nitroxide; ring-opening metathesis polymerization; star polymers; cancer

Imaging technologies have revolutionized clinical practice as well as drug discovery and development efforts.¹⁻⁴ For many imaging modalities, contrast agents (CAs) are used to improve signal-to-noise ratios (SNRs) for the detection of pathologic disease states.⁵⁻⁷ For example, ¹⁸F fluorodeoxyglucose (¹⁸F-FDG), iodine, as well as gadolinium chelates and iron oxide nanoparticles are among the most commonly utilized CAs for positron emission tomography (PET), computed tomography (CT), and magnetic resonance imaging (MRI), respectively.⁸⁻¹⁰ Among these imaging modalities, MRI enables noninvasive monitoring of disease progression at more frequent time intervals and minimizes patient exposure to ionizing radiation, which are key advantages.¹¹⁻¹⁵ MRI often suffers, however, from poor sensitivity, thus making CAs particularly useful in this context. The current generation of MRI CAs alter the relaxation time of surrounding water molecules in regions of interest (ROIs) via reduction of either the longitudinal relaxation time (T_1 contrast) or the transverse relaxation time (T_2 contrast).¹⁶⁻¹⁸ Note that some clinically utilized T_2 -based MRI CAs are metal-based nanoparticle formulations (e.g., superparamagnetic iron oxide nanoparticles (SPIONs)). While metal-based CAs have been shown to be generally nontoxic over short

time scales, chronic toxicity concerns remain for patients that require repeated or prolonged CA exposure.^{19–21} For example, studies as early as 2007 have demonstrated that gadolinium (Gd) chelates may be associated with nephrogenic systemic fibrosis (NSF); thus, their use has been prohibited in patients with renal insufficiency.^{22,23} Iron-based nanoparticle CAs (e.g., SPIONs), on the other hand, have also encountered safety concerns, leading to discontinuation of their development or withdrawal from the market.^{19,24,25} The only remaining United States Food and Drug Administration (FDA)-approved and available SPION is ferumoxytol, which continues to be used off-label as an MRI CA though it has its own safety concerns.^{19,24–27} Note that diagnostic CAs are held to a very high safety standard as they are often administered to healthy patients for disease screening.¹⁸ To date, the major design principle employed to overcome the toxicities of metal-based CAs has been to shorten their *in vivo* circulation times in order to minimize accumulation in otherwise healthy organs.^{28–30} While several metal-based CAs have been developed that have met these objectives, they are inherently not suitable for imaging over long time scales (e.g., several hours to days) as they are designed to clear rapidly from the body. The development of safer nanoparticle-based CAs that feature longer circulation times could enhance the signal-to-noise ratio (SNR) of MRI and allow for a higher uptake in tumor tissue and internalization by tumor cells, which could lead to applications such as monitoring of drug release.

It has been hypothesized that organic-based MRI CAs will be inherently safer than those based on metals and that they may provide opportunities for functional or responsive MR imaging (e.g., via codelivery of drug molecules or through leveraging the reactivity of organic molecules).^{31–34} This potential has driven several distinct approaches in the development of metal-free CAs. For example, ¹⁹F,^{35,36} hyperpolarized ¹³C,^{37,38} and chemical exchange saturation transfer (CEST)^{39,40} CAs have all shown promise for MRI; the use of these agents, however, often requires specific equipment and personnel with specialized training that do not currently exist in clinical settings. Alternatively, paramagnetic nitroxides represent a promising class of organic radical contrast agents (ORCAs)^{31,32} that are nontoxic and function via principles that are identical to those of current metal-based CAs. As such, an appropriately sensitive ORCA could potentially be integrated into existing clinical protocols to achieve safe long-term MRI contrast. Historically, the development of nitroxide-based ORCAs for MRI applications^{33,34} has been limited due to two critical weaknesses: (1) their low relaxivity (due to 1 unpaired electron per nitroxide as compared to 7 per Gd(III) or 5 per Mn(II) ion); and (2) their rapid *in vivo* reduction to diamagnetic hydroxylamines, which are MRI-inactive.⁴¹ Notably, the reducing properties of nitroxides have been exploited for several redox-based imaging applications on short time scales.^{42–44} In addition, progress toward the development of significantly more stable “reduction resistant” ORCAs has been made.^{45–48} Moreover, several groups have developed nitroxide-based MRI CAs⁴⁹ where nitroxides are incorporated into a multitude of scaffolds ranging from cyclodextrin⁵⁰ and lipids⁵¹ to polymeric systems,^{52–54} including polyurethane⁵⁵ or polyacetylene.⁵⁶ Despite such advances, these systems generally suffer from low water solubility, poor nitroxide reduction resistance, insufficient relaxivity, and/or a lack of *in vivo* optimization that precludes further development. Further clinical translation of ORCAs requires materials with improved circulatory half-lives, pharmacokinetic/

biodistribution profiles, stability, and MRI sensitivity. For example, to our knowledge, there are no examples of tumor detection using nitroxide-based CAs for MRI in translationally relevant *in vivo* models and over extended time scales.

Over the past several years, our group has developed brush-arm star polymers (BASPs) for applications that include combination drug delivery and molecular imaging.^{48,57–61} BASPs are prepared via “brush-first” ring-opening metathesis polymerization (ROMP),⁵⁷ which is a convergent and highly scalable process.⁶¹ BASPs carry a payload (e.g., drug or imaging agent) at the interface between a cross-linked core and a protective hydrophilic polyethylene glycol (PEG) shell. The payload is covalently attached to the BASP building blocks, which are branched macromonomers (MMs); BASPs with multiplexed functionality can be prepared in a simple “plug-and-play” fashion via mixing of different MMs at predetermined ratios.^{48,58–61} In addition, the cross-linked core can be engineered to be stimuli-responsive, enabling controlled release of therapeutic or imaging agents while leaving biodegradable and/or low mass byproducts.^{48,58–61} BASPs exhibit consistent *in vivo* properties, including pharmacokinetic and biodistribution profiles, that are independent of their payload.^{48,60,61} Moreover, their shells consist of PEGylated bottlebrush polymers, resulting in an extremely dense, hyperbranched nanoarchitecture that maintains a relatively small size (~30 nm) that enables accumulation in poorly permeable solid tumors.^{18,62,63} Finally, we emphasize that the major component of our BASPs is PEG, which is a commonly used biomaterial with acceptable safety characteristics over long time scales.^{18,24,61} BASP excretion profiles have been extensively examined in murine models, using fluorescence microscopy in conjunction with histopathological analyses, demonstrating elimination over several months.⁶¹

Despite the advances described above, all of our reported BASPs to date have been made by a synthetic approach that results in a single functional species per MM, which has limited the overall payload to ~5–10% by mass. In the context of MR imaging, while our previously reported BASP-ORCA1, which carries the reduction resistant cyclohexyl nitroxide (“chex”), displays high relaxivity and stability for a nitroxide-based ORCA, its low chex loading (6.4% w/w of conjugated species chex-N₃; see the Supporting Information (SI) for details) limits its imaging utility. While MRI of a simple subcutaneous tumor has been realized with this construct, such murine tumor models are inherently easy to visualize using nanomaterial constructs due to their exaggerated vascularity.⁴⁸ To translate a BASP-based ORCA to the clinic, a much higher chex loading is required in order to achieve a suitable molecular relaxivity at a lower dose, which in turn would require a complete redesign of the BASP synthetic approach. Such a redesign may enable the demonstration of effective contrast in orthotopic tumor models that better recapitulate human disease.

Here, we present an approach to BASP synthesis that enables a second generation of BASP-based ORCAs that overcome the above challenges. The strategy transforms a previously four-step linear synthesis, requiring four chromatography steps (43% overall yield on the ~0.1 g scale), to an overall three-step convergent synthesis (two-step longest linear sequence) that requires no chromatography and that provides our desired BASP precursor in 92% overall yield on the 100 g scale.⁶⁴ Most relevant to this work is the fact that this redesigned approach enables the iterative addition of payload to provide for conjugation of multiple chex groups per MM. These major breakthroughs in terms of scalability and

payload enhancement are deployed herein to prepare BASPs with three chex groups per repeat unit (BASP-ORCA3), which have a greatly increased mass fraction of chex (theoretical loading of conjugated species chex-N₃ in BASP-ORCA3 = 16.7% w/w). Due to this enhanced chex density and the retained relaxivity enhancement imparted by the BASP scaffold, BASP-ORCA3 features a very high r_2 transverse relaxivity of $>1000 \text{ mM}^{-1} \text{ s}^{-1}$ per BASP molecule, which is more than double that of the previous “gold standard” (BASP-ORCA1) for T_2 ORCAs.⁴⁸ Leveraging the modular nature of BASP synthesis, a secondary probe consisting of a near-infrared fluorophore (NIRF) may also be incorporated into BASP-ORCA3 to enable *in vivo* longitudinal detection of tumors via dual MR/optical imaging. The stability and safety of BASP-ORCA3 were examined, and its pharmacokinetic and biodistribution profiles were explored. BASP-ORCA3 generated stable T_2 contrast over a time scale that is relevant for translational applications (i.e., 24 h postinjection), which enabled highly sensitive *in vivo* MRI of tumors in two distinct murine models of human cancer (subcutaneous plasmacytomas and disseminated ovarian tumor implants). In addition to achieving selective visualization of large subcutaneous tumors as well as small ($<5 \text{ mm}$) tumors in the disseminated model, BASP-ORCA3 allowed for detailed mapping of tumor architectural features with potential prognostic significance (e.g., the presence of tumor necrosis that correlates with therapeutic outcomes and tumor activity).

RESULTS AND DISCUSSION

To maximize the relaxivity of BASP-ORCAs, we sought to increase chex loading without otherwise altering the physical properties or the optimized sizes of the resultant constructs. To achieve this goal, MMs with one, two, or three alkyne functional handles were prepared;⁶⁴ reduction-resistant chex-N₃ molecules were then appended to these MMs via copper-catalyzed azide-alkyne cycloaddition to provide mono-, bis-, and tris-chex MMs (chex_{*x*}-MM, $x = 1, 2, 3$). Matrix-assisted laser desorption ionization time-of-flight (MALDI-TOF) mass spectra (Figures S1–S3) and double integration (spin counting) of the electron paramagnetic resonance (EPR) spectra of chex_{*x*}-MM, $x = 1–3$ (Figure S4) supported the presence of one, two, and three nitroxides, respectively. Notably, the theoretical mass fraction of chex-N₃ increases significantly with x : from 9.4% w/w ($x = 1$) to 22.6% ($x = 3$) w/w, which is the key to realizing high molecular relaxivity of BASPs in this work (*vide infra*).

BASP-ORCAs were synthesized from the corresponding chex_{*x*}-MMs, using brush-first ROMP (Figure 1).^{48,57–60} For BASP candidates that were intended to be used for *in vivo* studies, a NIRF-conjugated MM (Cy-MM; 1 mol %) was also incorporated to enable *in vivo* tracking of the resulting BASP-ORCAs by both MRI (high resolution) and *in vivo* optical imaging (high sensitivity).⁴⁸ Due to the ratiometric control that is provided by the convergent brush-first ROMP method, this dual imaging capability was readily achieved despite large differences in the concentration requirements for effective tissue enhancement that are inherent to the 2 different types of CAs (i.e., mM to μM for MRI and nM to pM for NIRF imaging).⁶⁵ BASP-ORCAs with brush lengths (m) of 7–10 and cross-linker equivalences (N) of 20–30 were examined for doubly and triply loaded chex_{*x*}-MMs ($x = 2–3$) (Table S1); these conditions have previously been shown to yield BASPs of optimal size and aqueous solubility for *in vivo* applications.^{48,57–60} Gel permeation chromatography

(GPC) traces acquired from reaction mixtures revealed good MM-to-brush and brush-to-BASP conversion in all cases (90% and 80%, respectively, Table S1, Figure S5). Moreover, for these m and N values, BASP-ORCAs with diameters of 25–51 nm (as determined by dynamic light scattering (DLS) and transmission electron microscopy (TEM)) were obtained (Table S1, Figure 2A,B). Based on a combination of size (hydrodynamic diameter = 29 ± 10 nm) and relaxivity considerations (*vide infra*), we chose the BASP-ORCA with $x = 3$, $m = 7$, and $N = 20$ (hereafter referred to as BASP-ORCA3) for further development. The progression from single- to double and triple-loading of chex in this system was included to demonstrate the well-behaved and modular characteristics of our platform. In the context of translational applications, we decided to focus on BASP-ORCA3 due to its highest nitroxide density and associated molecular relaxivity.

We compared the EPR spectra of chex $_x$ -MM ($x = 1, 2, 3$) to that of the resultant BASP-ORCA to gain a better understanding of how increasing chex density in our materials impacts the nitroxide environment. Computational fitting of the EPR spectra for chex $_x$ -MM showed that increasing x led to longer correlation times for rotational diffusion and increased internitroxide interactions, which reflects the increased molecular size and chex density of these MMs (Figure S4). Compared to its constituent MM (chex $_3$ -MM), the EPR spectrum of BASP-ORCA3 was extensively broadened; three well-resolved peaks for chex $_3$ -MM merged into one broad peak for BASP-ORCA3 (Figure 2C). Longitudinal (r_1) and transverse (r_2) relaxivities of BASP-ORCAs as a function of m , N , and x were measured and compared; the per chex values for both r_1 and r_2 were not altered upon single-, double-, or triple-loading ($x = 1, 2$, or 3 respectively) of chex groups (Table S1).^{47,48} Most importantly, the large enhancement in r_2 upon incorporation of chex observed previously for BASP-ORCA1 was retained;⁴⁸ BASP-ORCA3 exhibited a per chex r_2 value of $4.62 \text{ mM}^{-1} \text{ s}^{-1}$, which is similar to BASP-ORCA1 ($4.67 \text{ mM}^{-1} \text{ s}^{-1}$)⁴⁸ and a ~ 27 -fold enhancement compared to the value obtained for the benchmark nitroxide 3-CP (Table S1). In addition, BASP-ORCA3 features a high chex loading (16.7% w/w; 0.474 mmol chex/g theoretical and 0.473 mmol/g measured; 99.7% spin concentration as measured by EPR spectroscopy), good water solubility (>100 mg/mL), and an optimal size range (29 ± 10 nm by DLS, 43 ± 8 nm by TEM) for prolonged *in vivo* circulation and passive tumor accumulation and penetration.^{66,67}

As estimated from the molar mass obtained by GPC with static light scattering, BASP-ORCA3 ($M_w = 6.6 \times 10^5$ Da, $\text{PDI} = 1.34$) contains >200 chex groups, resulting in a molecular r_2 value of $>1000 \text{ mM}^{-1} \text{ s}^{-1}$ at 7 T. Compared to BASP-ORCA1 (molecular $r_2 \sim 450 \text{ mM}^{-1} \text{ s}^{-1}$ at 7 T),⁴⁸ this exceptionally high relaxivity suggested that BASP-ORCA3 would display significantly greater MRI contrast at the same concentration. To test this hypothesis, we compared the performance of BASP-ORCA3 and BASP-ORCA1 as T_2 contrast agents, using MRI phantoms. Indeed, BASP-ORCA3 displayed greater contrast than BASP-ORCA1 at all examined equivalent w/v concentrations (Figures 3A and S6). We further compared their imaging sensitivity via incubation of BASP-ORCA3 and BASP-ORCA1 with clusters of MM.1S cells, which are derived from an established multiple myeloma cell line, in order to determine the minimal cluster size that is detectable by MRI (Figure 3B). Note that this detection parameter is a more relevant criterion for the intended use of CAs for *in vivo* tumor identification by MRI. A cluster of 500 MM.1S cells incubated with BASP-ORCA3

resulted in a ~9.7% amplification in contrast enhancement, which increased linearly to ~24.8% for 50,000 cells; BASP-ORCA1, on the other hand, exhibited <10% enhancement at all examined conditions (Figure 3B).

To test whether the redesigned BASP nanostructure could still effectively shield the increased payload of chex from reduction by common biological reducing agents, BASP-ORCA3 was exposed to excess ascorbate (Asc) and glutathione (GSH).^{41,68} We compared the reduction kinetics as measured by EPR spectroscopy of BASP-ORCA1 and BASP-ORCA3 at constant equivalency of reducing agents per chex molecule; in other words, BASP-ORCA3 was exposed to a 3-fold higher concentration of reducing agents. Despite this difference, the extent of chex reduction remained the same between BASP-ORCA1 and BASP-ORCA3 (Figures S7 and S8, Table S2), suggesting that the installation of 3-fold more chex onto BASP-ORCA3 did not compromise chex stability. Note that BASP-ORCA1 has been demonstrated to provide sufficient nitroxide stability *in vivo*;⁴⁸ hence, it was used in the current study as the benchmark for stability evaluation. The reduction process was also monitored by NIRF spectroscopy (Figures S9 and S10) to determine if the larger chex density of BASP-ORCA3 led to increased fluorescence quenching.⁶⁹ An increase of ~60% fluorescence intensity was observed upon chex reduction, suggesting minimal fluorescence quenching compared to our previously reported bottlebrush polymer (Figure S10).⁴⁷ Given the increased nitroxide payload of BASP-ORCA3, this finding is consistent with the ~30% increase in fluorescence intensity that has been observed in BASP-ORCA1 with similar kinetics.⁴⁸ Taken together, these data strongly suggest that the incorporation of 3-fold greater nitroxide density in BASP-ORCA3 provides a large increase in molecular relaxivity without compromising the beneficial features of the BASP design (e.g., size control, stability, limited fluorescing quenching) that are critical to its *in vivo* performance.

Having established the basic contrast enhancement and physical properties of BASP-ORCA3, we further evaluated its performance in biological systems. *In vitro* cytotoxicity experiments were conducted by incubating BASP-ORCA3 at varying concentrations with different established cell lines: MM.1S, OVCAR8 (high-grade serous ovarian cancer), and HUVEC (human umbilical vein endothelial cells). Note that MM.1S and OVCAR8 cells were also employed to generate our *in vivo* model systems (*vide infra*); HUVEC cells were selected as a highly toxin-sensitive *in vitro* model system and to examine potential *in vivo* vascular toxicities that could be imparted by BASP-ORCA3. After 72 h of continuous *in vitro* exposure, which mimicked expected *in vivo* behavior during intravascular circulation and tumor extravasation,^{48,60} cell viability was determined by the CellTiter-Glo assay. The half-maximal inhibitory concentration (IC₅₀) values of BASP-ORCA3 to affect the viability of MM.1S, OVCAR8, and HUVECs were 3.17, 3.81, and 8.12 mg/mL, respectively (Figure S11), suggesting negligible *in vitro* toxicity at practical concentrations. To evaluate the *in vivo* safety profile of BASP-ORCA3, we administered the agent via either intravenous (iv) or intraperitoneal (ip) injection to healthy balb/c mice at a fixed dose of 30 mg (1.5 g/kg, *n* = 3 mice); the mice were euthanized 24 h later and their organs were excised for histological analyses after hematoxylin and eosin (H&E) staining. No signs of gross architectural distortion were observed in any major organ, including the lungs, liver, spleen, heart, and kidneys (Figure S12). These results were consistent with the well-known tolerability of

PEG^{18,66} and nitroxide-based^{31–34} materials, supporting the further examination of other *in vivo* performance characteristics of BASP-ORCA3.

The pharmacokinetic (PK) and biodistribution (BD) profiles of our BASP-ORCAs were evaluated by NIRF-based optical imaging, using an IVIS Imaging System with gating on the fluorescence of ROIs in the Cy5.5 channel ($\lambda_{\text{ex}}/\lambda_{\text{em}} = 640/700$ nm). Balb/c mice were administered BASP-ORCA3 by either iv ($n = 3$ mice) or ip injection ($n = 3$ mice) (Figures S13 and S14). For determination of PK parameters, blood samples were collected at predetermined time points for up to 72 h after administration. The blood samples were imaged *ex vivo*, using the IVIS instrument and the same imaging parameters as described above. The percent injected dose (%ID) was plotted as a function of time and fitted to a standard two-compartment model⁷⁰ (Figures S13 and S14), yielding a blood-compartment half-life of 13 h (after ip administration) and 26 h (upon iv injection). BASP-ORCA3 exhibited PK behavior consistent with other hyper-branched PEG-based nanomaterials.^{48,71} It was cleared mainly through the liver with a minor contribution from the kidneys, allowing for the potential use of this nonmetal-based ORCA in patients with compromised renal function.

Having demonstrated the high tolerability and favorable *in vivo* PK/BD of BASP-ORCA3, its contrast sensitivity for *in vivo* T_2 -enhanced MRI of tumors was examined. BASP-ORCA3 was evaluated in the context of a subcutaneous xenograft model of multiple myeloma, which is an incurable plasma cell dyscrasia that can lead to lytic bone lesions, defective hematopoiesis, and renal failure.⁷² SCID mice were injected with 2.0×10^6 MM.1S cells in the flank, establishing a plasmacytoma (*i.e.*, a clinically observed extramedullary tumor that consists of multiple myeloma cells); the tumor of each mouse was allowed to grow to >1 cm in diameter. Randomized groups of tumor-bearing mice ($n = 4$) were then administered either BASP-ORCA3 or BASP-ORCA1 by iv injection and were imaged by MRI and NIRF-based optical imaging after 24 h. Qualitatively, mice in the two treatment groups displayed similarly efficient accumulation of CAs at tumor sites as well as similar BD profiles (Figures 4A and S15). Quantitative analysis of T_2 MR images of tumors revealed $12.4 \pm 0.4\%$ and $24.3 \pm 0.7\%$ ($p < 0.05$) contrast enhancement for mice injected with BASP-ORCA1 and BASP-ORCA3, respectively (Figure 4B,C).

We observed that necrotic tumor regions experienced greater contrast enhancement (Figure 4B). These contrast changes reached $28.2 \pm 2.7\%$ for BASP-ORCA1 and $69.1 \pm 3.6\%$ for BASP-ORCA3 ($p < 0.05$) (Figure 4C). In order to evaluate the basis for the difference in intratumoral contrast enhancement, the treated tumors were excised; analyses were performed on parallel sections by light microscopy after H&E staining to evaluate tissue histology; and, fluorescence microscopy was conducted to visualize the locations of the NIRF-containing CAs, revealing the specific accumulation of BASP-ORCAs in necrotic tumor regions (Figure 4D). While both BASP-ORCAs exhibited this behavior quantitatively (Figure 4C), this information went previously unnoticed due to the relatively lower relaxivity of BASP-ORCA1 (Figure 4B). Upon examination of the data in total, BASP-ORCA3 outperformed BASP-ORCA1 with respect to its contrast enhancement capabilities and clearly deciphered the presence of necrotic tumor regions. With respect to the latter phenomenon, tumor necrosis commonly occurs in large subcutaneous tumors and especially

tumors composed of MM.1S cells.⁷³ The presence of necrotic sites induces enhanced vascular permeability but limits parenchymal tumor diffusion,⁶⁶ which, in turn, causes BASP-ORCAs to passively accumulate in perivascular spaces to a greater degree. This finding strongly advocates for the use of BASP-ORCA3 as an effective diagnostic tool for the detection of tumor necrosis, which is an important prognostic biomarker that is connected to various pathological states as well as to treatment outcomes, including the efficacy of radiation and cytotoxic drug therapy.⁷⁴

As it was important to confirm that the observed enhancements in MRI contrast were due to a higher chex density rather than to any improvements in tumor accumulation for BASP-ORCA3 as compared to BASP-ORCA1, major organs from the same mice were harvested at the time of animal sacrifice (after imaging), homogenized, and characterized by EPR spectroscopy (to quantify chex radical concentration), by IVIS (to quantify NIRF content), and by the bicinchoninic acid assay (BCA assay; to measure the protein concentration in tissue samples). While the BD profiles of the two different BASP-ORCAs were similar as observed by NIRF-based imaging, EPR quantification revealed higher concentrations of chex in the various organs of animals injected with BASP-ORCA3, which is consistent with a higher density of chex on a per BASP basis (Figure S16). The chex concentration in the tumor was $0.68 \pm 0.18 \mu\text{mol chex/g protein}$ for BASP-ORCA3, which is significantly higher than the $0.17 \pm 0.04 \mu\text{mol chex/g protein}$ measured from the tumors of animals that had been administered BASP-ORCA1 ($p < 0.05$, 3.0–4.8% ID/g protein); these values are in good agreement with the differences in contrast enhancement that were observed *in vivo*, *vide supra* (Figures 4C and S16A).

To further evaluate BASP-ORCA3 as a tumor imaging platform, its threshold to detect minute tumor deposits was explored. For these studies, a murine model of advanced-stage and high grade serous ovarian cancer (HGSOC), consisting of intraperitoneal dissemination of OVCAR8 cells into nude mice, was employed; this model system exhibits a fast tumor growth rate, lower tumor vascularization, and the propensity to establish tumor implants on the serosal surfaces of peritoneal organs that range in size from 1 to 5 mm and that display similar metastatic patterns, genetic profiles, and histologic features to those of human HGSOCs.^{71,75} BASP-ORCAs were introduced into animals by ip injection, which is a clinically relevant mode of therapeutic administration in advanced-stage ovarian cancer that has been shown to promote marked accumulation of PEG-based nanomaterials in ovarian tumors for imaging and/or therapy.^{71,75,76} For this current study, NCR-NU mice ($n = 5$) were injected with OVCAR8 cells transfected with firefly luciferase, allowing for facile monitoring of the *in vivo* dissemination and tumor growth via bioluminescence imaging (BLI) (Figure 5A). The tumor implants were allowed to establish for 22 days; mice were then randomized into groups with equivalent tumor burden. The animals were administered either BASP-ORCA3 or BASP-ORCA1 by ip injection. After 24 h, the mice were imaged by BLI, NIRF-based optical imaging, and MRI (Figures 5A–C and S17). Qualitatively, BASP-ORCAs (as monitored by NIRF-based optical imaging; Cy5.5) colocalized with OVCAR8 tumors (as visualized by BLI). Leveraging the high-resolution imaging capabilities of MRI, BASP-ORCAs were found to further enhance contrast sensitivity and enabled ready visualization of small tumor implants in T_2 -weighted MR images (Figure 5C,D). Quantitative analysis revealed contrast enhancements of $14.3 \pm 0.9\%$ for BASP-

ORCA1 and $33.6 \pm 4.4\%$ for BASP-ORCA3 ($p < 0.05$; Figure 5E), which corresponded to a 2.3-fold improvement in sensitivity with BASP-ORCA3 as compared to its predecessor. Notably, this difference in contrast was consistent with the 2.6-fold increased payload of chex by weight for BASP-ORCA3.

Upon completion of the *in vivo* imaging studies, the organs of the mice were processed as previously described for the subcutaneous MM.1S model (*vide supra*) to confirm that the observed differences in contrast enhancement were again due to increased chex density (Figure 6). Indeed, the chex concentration in the organs of animals that were administered BASP-ORCA3 was generally higher than in those that were administered BASP-ORCA1 (Figure 6B). In tumor tissue, a chex concentration of $2.63 \pm 0.61 \mu\text{mol chex/g protein}$ was observed for animals in the BASP-ORCA3 group, whereas the tumors of mice that received BASP-ORCA1 possessed $1.00 \pm 0.27 \mu\text{mol chex/g protein}$ ($p < 0.05$; Figure 6B). NIRF-based optical imaging confirmed that these differences were due to the increased density of chex in BASP-ORCA3 when compared to BASP-ORCA1, as opposed to differences in the accumulation of these two particles in tumor tissues (Figure 6C). The observed tumor uptake was similar to that of other polymers that were introduced via the same injection route (ip) into this tumor model.^{71,76} We also note that, throughout both tumor imaging studies, the BD profiles of the BASP-ORCAs (Figures S15 and S17), which were determined by quantification of NIRF and EPR signals in *ex vivo* organ homogenates, were consistent with the BD/PK data acquired in the non-tumor-bearing balb/c mice (Figure S13 and S14), supporting the generalizability of our findings for immunocompetent subjects.

CONCLUSIONS

We report a new family of nanoparticles with an exceptionally high nitroxide density. Brush-first ROMP of a triply loaded chex MM (chex₃-MM) produced a macromolecular construct, BASP-ORCA3, that features the highest payload of MRI-active chex that has been reported to date. In concert with our BASP nanoarchitecture, this high chex density imparts outstanding molecular transverse relaxivity while preserving exceptional *in vivo* stability. Due to its very high chex payload, BASP-ORCA3 addresses the low contrast that has, thus far, hindered the successful translational development of nitroxide-based MRI CAs. Of particular interest is the ability of BASP-ORCA3 to heterogeneously distribute within tumors, specifically identifying necrotic regions that may serve as important biomarkers (e.g., for radiation resistance). Coupled with the facile ability to prepare BASPs with combinations of different therapeutic agents,^{58–61,77,78} these architectures may provide tools for image-guided drug delivery and/or real-time evaluation of therapeutic efficacy. As demonstrated in an orthotopic murine model of disseminated human ovarian cancer with high clinical relevance, BASP-ORCA3 is able to generate an enhanced T_2 signal even within poorly vascularized tumor deposits, which enables ready detection of millimetric tumors by MRI. Taken together, these data illustrate the translational potential of BASP-ORCA3 for applications in early cancer diagnosis and longitudinal therapeutic monitoring. Our work further supports the development of nitroxide-based CAs as an alternative to current metal-based agents for clinical imaging applications.

METHODS

Synthesis of BASP-ORCAs.

Note: All BASP-ORCA syntheses were performed in a glovebox under N_2 atmosphere; however, similar results are expected under ambient conditions. All ROMP reactions followed the same general procedure, which was modified from reported examples.^{48,58,59}

Representative procedure for BASP-ORCA synthesis with brush length of 7.07 (m) and 20 equiv (N) of cross-linker (BASP-ORCA3, $x = 3$, $m = 7.07$, $N = 20$): To a 4 mL vial, a suspension of Acetal-XL (12.2 mg, 21.0 μmol , 20.0 equiv) in THF (209.7 μL , 0.1 M Acetal-XL) was prepared. To a second 4 mL vial containing a stir bar, chex₃-MM (34.0 mg, 7.3 μmol , 7.0 equiv) was added; Cy-MM was then added from a premade 12.5 mg/mL solution in THF (24.0 μL , 0.073 μmol , 0.07 equiv). To a third vial, a solution of Grubbs 3rd generation bispyridyl catalyst (G3-cat, 0.02 M in THF) was freshly prepared. THF (71.9 μL) was then added to the MM vial, followed by the addition of G3-cat solution (52.4 μL , 1.0 μmol , 1.0 equiv) to give the desired MM/ G3-cat ratio of 7.07:1 (1 mol % of the Cy-MM), while achieving a total MM concentration of 0.05 M. The dark blue reaction mixture was allowed to stir for 30 min at room temperature before an aliquot ($\sim 5 \mu\text{L}$) was taken out and quenched with 1 drop of ethyl vinyl ether for GPC analysis. The Acetal-XL suspension was then added dropwise (in aliquots of 5 equiv, or $\sim 50 \mu\text{L}$, every 5 min) over the course of 20 min into the reaction vial, and the dark blue polymerization was allowed to proceed for 6 h at room temperature while stirring. To quench the polymerization, a drop of ethyl vinyl ether was added. The reaction mixture was transferred to 8 kDa molecular weight cutoff dialysis tubing (Spectrum Laboratories) in 5 mL nanopure water, and the solution was dialyzed against H₂O (500 mL \times 3, solvent exchange every 6 h). The dialyzed solution of BASP-ORCA3 was then concentrated to the desired concentration via centrifugation with a filter tube (100 kDa MWCO, Millipore Sigma).

In Vivo MR and NIRF Image Acquisition.

In vivo MR images of the subcutaneous multiple myeloma model were obtained by using a 7T Bruker BioSpec USR70/30 instrument that is housed in the Lurie Imaging Facility Center at the Dana-Farber Cancer Institute (DFCI); *in vivo* MR images of the disseminated xenograft model of advanced-stage ovarian cancer were acquired using a Varian 7T/310/ASR-whole mouse MRI system housed in the Koch Institute for Integrative Cancer Research at MIT. Scans were collected with respiratory gating (PC-SAM version 6.26 by SA Instruments Inc.) to avoid noise due to chest movement. The respiratory rate and animal temperature were closely monitored during image acquisition. Coronal T_2 weighted images (T_2 WIs) were collected by employing the fast spin echo multiple slices pulse sequence with $T_R = 4000$ ms; $T_{E(\text{eff})} = 48$ ms; ETL = 8; FOV = 100×50 mm²; 512×256 matrix and 2 averages over 20–30 slices (to capture a maximum number of tumors) that were of 0.5 mm thickness and 0.5 mm gap. Axial T_2 WIs were collected using the fast spin echo multiple slices pulse sequence with $T_R = 4000$ ms; $T_{E(\text{eff})} = 48$ ms; ETL = 8; FOV = 45×45 mm²; 256×192 matrix and 2 averages over 20–30 slices (to capture the entire tumor) at 1 mm thickness and 1 mm gap. *In vivo* NIRF-based optical images were obtained by using identical IVIS bioluminescence and fluorescence imaging systems (Xenogen) housed in the DFCI and MIT facilities. Epifluorescence imaging was acquired through excitation of the

Cy5.5 fluorophore ($\lambda_{\text{ex}}/\lambda_{\text{em}} = 640/700$ nm, exposure time 2–10 s) incorporated within the BASP-ORCAs. Imaging of subcutaneous plasmacytomas was performed with animals placed on their sides so that their tumors faced the camera; imaging of the disseminated ovarian cancer model was performed with animals in the prone position.

***In Vivo* MR and NIRF-Based Optical Imaging of Tumor-Bearing Mice.**

Tumor cells for animal implantation were cultured to a final concentration of 20% (see the SI for details). Cells were then harvested, resuspended in sterile pH 7.4 PBS buffer, passed through sterile 0.2 μm filters, and injected accordingly. MRI and NIRF-based optical images were acquired for each animal before injection. BASP-ORCA solutions (30 mg in PBS, injected as 0.25 mL of a 120 mg/mL solution, 0.22 mmol chex/kg for BASP-ORCA1; 0.57 mmol chex/kg for BASP-ORCA3) were prepared, passed through a sterile 0.2 μm filter, and administered to the tumor-bearing mice via iv (subcutaneous model) or ip injection (orthotopic model). Tumor imaging by MRI and NIRF-based optical imaging was conducted 24 h thereafter. Mice were then immediately euthanized in a CO_2 chamber; their organs were collected, imaged, and stored in dry ice for EPR analysis.

***Ex Vivo* EPR Spectroscopy.**

Harvested organs were shipped on dry ice to the University of Nebraska, where they were stored at -80 °C. For EPR sample preparation, each tissue sample, one at a time, was rapidly thawed and transferred to a weighed vial; 900 μL of PBS buffer (0.5 mM, pH 7.2) were then added. The mixture was put into an ice–water bath and homogenized with a rotor stator homogenizer; it was then pipeted into a 4 mm outer diameter EPR sample tube. The samples were degassed by sonication as needed (for instance, when gas bubbles were visible). The EPR tube was capped, sealed with parafilm, and stored briefly in an acetone/dry ice bath before spin concentration measurements. Spin concentrations of nitroxide radicals in tissues (μmol chex per g protein; *Note*: see the SI for details of protein content determination) were measured at -30 °C (243.2 K) to increase signal-to-noise of the aqueous samples. Measurements of tissue samples were alternated with that of the spin concentration reference and *g*-value reference. For tissue samples with low signal-to-noise, the cavity background was recorded with identical parameters, including numbers of scans and receiver gain. Typical parameters were as follows: microwave attenuation, 20 dB; modulation amplitude, 5 Gauss; spectral width, 300 Gauss; resolution, 512 points; conversion, 40.96; time constant, 10.24; and sweep time, 20.97 s. These parameters were kept identical for the tissues, references, and cavity backgrounds. The number of scans (8–256) and receiver gain were adjusted as needed for each sample. The reference for spin concentration was 0.50 mM Proxyl in PBS (pH 7.2). This reference was always stored in dry ice, except during measurements, and occasionally rechecked for spin concentration decay. The *g*-value reference was 2,2-diphenyl-1-picrylhydrazyl powder.

Supplementary Material

Refer to Web version on PubMed Central for supplementary material.

ACKNOWLEDGMENTS

We thank the NIH-NCI (1R01CA220468-01 for J.A.J., P.P.G., A.R., A.J.), the NIH-NIBIB (R01 EB-019950-01A1 for A.R.), the NIH (U01-NS090451 for A.J.), and the National Science Foundation (Graduate Research Fellowship for H.V.-T.N.) for support of this research. A.D. acknowledges support from the Fondation Francaise pour la Recherche contre le Myelome et les Gammopathies, the Philippe Foundation, and the Multiple Myeloma Research Foundation. P.H. acknowledges support from a Wellcome Trust-MIT Postdoctoral Fellowship. PPG acknowledges the support of the Charles W. and Jennifer C. Johnson Clinical Investigator Fund and of the Kathryn Fox Samway Foundation. This work was supported in part by the Koch Institute Support (core) Grant P30-CA14051 from the National Cancer Institute. We thank the Koch Institute Swanson Biotechnology Center for technical support, specifically Dr. W. Huang.

REFERENCES

- (1). Weissleder R Molecular Imaging in Cancer. *Science* 2006, 312, 1168–1171. [PubMed: 16728630]
- (2). Willmann JK; van Bruggen N; Dinkelborg LM; Gambhir SS Molecular Imaging in Drug Development. *Nat. Rev. Drug Discovery* 2008, 7, 591–607. [PubMed: 18591980]
- (3). Mankoff DA; Pryma DA; Clark AS Molecular Imaging Biomarkers for Oncology Clinical Trials. *J. Nucl. Med* 2014, 55, 525–528. [PubMed: 24614222]
- (4). Shankar LK The Clinical Evaluation of Novel Imaging Methods for Cancer Management. *Nat. Rev. Clin. Oncol* 2012, 9, 738–744. [PubMed: 23149888]
- (5). Viola KL; Sbarboro J; Sureka R; De M; Bicca MA; Wang J; Vasavada S; Satpathy S; Wu S; Joshi H; Velasco PT; MacRenaris K; Waters EA; Lu C; Phan J; Lacor P; Prasad P; Dravid VP; Klein WL Towards Non-Invasive Diagnostic Imaging of Early-Stage Alzheimer's Disease. *Nat. Nanotechnol* 2015, 10, 91–98. [PubMed: 25531084]
- (6). Fischer B; Lassen U; Mortensen J; Larsen S; Loft A; Bertelsen A; Ravn J; Clementsen P; Hogholm A; Larsen K; Rasmussen T; Keiding S; Dirksen A; Gerke O; Skov B; Steffensen I; Hansen H; Vilman P; Jacobsen G; Backer V; et al. Preoperative Staging of Lung Cancer with Combined PET-CT. *N. Engl. J. Med* 2009, 361, 32–39. [PubMed: 19571281]
- (7). Dimopoulos M; Terpos E; Comenzo RL; Tosi P; Beksac M; Sezer O; Siegel D; Lokhorst H; Kumar S; Rajkumar SV; Niesvizky R; Moulopoulos LA; Durie BG IMWG. International Myeloma Working Group Consensus Statement and Guidelines Regarding the Current Role of Imaging Techniques in the Diagnosis and Monitoring of Multiple Myeloma. *Leukemia* 2009, 23, 1545–1556. [PubMed: 19421229]
- (8). Dammacco F; Rubini G; Ferrari C; Vacca A; Racanelli V 18F-FDG PET/CT: a Review of Diagnostic and Prognostic Features in Multiple Myeloma and Related Disorders. *Clin. Exp. Med* 2015, 15, 1–18. [PubMed: 25218739]
- (9). Lusic H; Grinstaff MW X-Ray-Computed Tomography Contrast Agents. *Chem. Rev* 2013, 113, 1641–1666. [PubMed: 23210836]
- (10). Xiao YD; Paudel R; Liu J; Ma C; Zhang ZS; Zhou SK MRI Contrast Agents: Classification and Application. *Int. J. Mol. Med* 2016, 38, 1319–1326. [PubMed: 27666161]
- (11). O'Connor JP; Aboagye EO; Adams JE; Aerts HJ; Barrington SF; Beer AJ; Boellaard R; Bohndiek SE; Brady M; Brown G; Buckley DL; Chenevert TL; Clarke LP; Collette S; Cook GJ; deSouza NM; Dickson JC; Dive C; Evelhoch JL; Faivre-Finn C; et al. Imaging Biomarker Roadmap for Cancer Studies. *Nat. Rev. Clin. Oncol* 2017, 14, 169–186. [PubMed: 27725679]
- (12). Shapiro MG; Westmeyer GG; Romero PA; Szablowski JO; Kuster B; Shah A; Otey CR; Langer R; Arnold FH; Jasanoff A Directed Evolution of a Magnetic Resonance Imaging Contrast Agent for Noninvasive Imaging of Dopamine. *Nat. Biotechnol* 2010, 28, 264–270. [PubMed: 20190737]
- (13). Mi P; Kokuryo D; Cabral H; Wu H; Terada Y; Saga T; Aoki I; Nishiyama N; Kataoka K A pH-Activatable Nanoparticle with Signal-Amplification Capabilities for Non-Invasive Imaging of Tumour malignancy. *Nat. Nanotechnol* 2016, 11, 724–730. [PubMed: 27183055]
- (14). Harrison VSR; Carney CE; MacRenaris KW; Waters EA; Meade TJ Multimeric Near IR-MR Contrast Agent for Multimodal In Vivo Imaging. *J. Am. Chem. Soc* 2015, 137, 9108–9116. [PubMed: 26083313]

- (15). Detappe A; Kunjachan S; Sancey L; Motto-Ros V; Biancur D; Drane P; Guieze R; Makrigiorgos GM; Tillement O; Langer R; Berbeco R Advanced Multimodal Nanoparticles Delay Tumor Progression with Clinical Radiation Therapy. *J. Controlled Release* 2016, 238, 103–113.
- (16). Caravan P; Ellison JJ; McMurry TJ; Lauffer RB Gadolinium(III) Chelates As MRI Contrast Agents: Structure, Dynamics, and Applications. *Chem. Rev* 1999, 99, 2293–352. [PubMed: 11749483]
- (17). Sun C; Lee JS; Zhang M Magnetic Nanoparticles in MR Imaging and Drug Delivery. *Adv. Drug Delivery Rev* 2008, 60, 1252–1265.
- (18). Smith BR; Gambhir SS Nanomaterials for In Vivo Imaging. *Chem. Rev* 2017, 117, 901–986. [PubMed: 28045253]
- (19). Wang YX Superparamagnetic Iron Oxide Based MRI Contrast Agents: Current Status of Clinical Application. *Quant. Imaging Med. Surg* 2011, 1, 35–40. [PubMed: 23256052]
- (20). Nardone B; Saddleton E; Laumann AE; Edwards BJ; Raisch DW; McKoy JM; Belknap SM; Bull C; Haryani A; Cowper SE; Abu-Alfa AK; Miller FH; Godinez-Puig V; Dharnidharka VR; West DP Pediatric Nephrogenic Systemic Fibrosis is Rarely Reported: a RADAR Report. *Pediatr. Radiol* 2014, 44, 173–180. [PubMed: 24057195]
- (21). Wang YX Current Status of Superparamagnetic Iron Oxide Contrast Agents for Liver Magnetic Resonance Imaging. *World J. Gastroenterol* 2015, 21, 13400–13402. [PubMed: 26715826]
- (22). Perazella MA Current Status of Gadolinium Toxicity in Patients with Kidney Disease. *Clin. J. Am. Soc. Nephrol* 2009, 4, 461–469. [PubMed: 19201920]
- (23). Kanda T; Fukusato T; Matsuda M; Toyoda K; Oba H; Kotoku J; Haruyama T; Kitajima K; Furui S Gadolinium-Based Contrast Agent Accumulates in the Brain Even in Subjects without Severe Renal Dysfunction: Evaluation of Autopsy Brain Specimens with Inductively Coupled Plasma Mass Spectroscopy. *Radiology* 2015, 276, 228–232. [PubMed: 25942417]
- (24). Thakor AS; Jokerst JV; Ghanouni P; Campbell JL; Mittra E; Gambhir SS Clinically Approved Nanoparticle Imaging Agents. *J. Nucl. Med* 2016, 57, 1833–1837. [PubMed: 27738007]
- (25). Pierre VC; Allen MJ; Caravan P Contrast Agents for MRI: 30+ Years and Where Are We Going? *JBIC, J. Biol. Inorg. Chem* 2014, 19, 127–131. [PubMed: 24414380]
- (26). Vasanawala SS; Nguyen K-L; Hope MD; Bridges MD; Hope TA; Reeder SB; Bashir MR Safety and Technique of Ferumoxytol Administration for MRI Magn. Magn. Reson. Med 2016, 75, 2107–2111. [PubMed: 26890830]
- (27). FDA Drug Safety Communication: FDA strengthens warnings and changes prescribing instructions to decrease the risk of serious allergic reactions with anemia drug Feraheme (ferumoxytol); U.S. Food & Drug Administration (FDA), 2015; <https://www.fda.gov/Drugs/DrugSafety/ucm440138.htm> (accessed Oct 17, 2018).
- (28). Li Y; Lin TY; Luo Y; Liu Q; Xiao W; Guo W; Lac D; Zhang H; Feng C; Wachsmann-Hogiu S; Walton JH; Cherry SR; Rowland DJ; Kukis D; Pan C; Lam KS A Smart and Versatile Theranostic Nanomedicine Platform Based on Nanoporphyrin. *Nat. Commun* 2014, 5, 4712. [PubMed: 25158161]
- (29). Detappe A; Kunjachan S; Drane P; Kotb S; Myronakis M; Biancur DE; Ireland T; Wagar M; Lux F; Tillement O; Berbeco R Key Clinical Beam Parameters for Nanoparticle-Mediated Radiation Dose Amplification. *Sci. Rep* 2016, 6, 34040. [PubMed: 27658637]
- (30). Perez-Balderas F; van Kasteren SI; Aljabali AA; Wals K; Serres S; Jefferson A; Sarmiento Soto M; Khrapitchev AA; Larkin JR; Bristow C; Lee SS; Bort G; De Simone F; Campbell SJ; Choudhury RP; Anthony DC; Sibson NR; Davis BG Covalent Assembly of Nanoparticles as a Peptidase-Degradable Platform for Molecular MRI. *Nat. Commun* 2017, 8, 14254. [PubMed: 28198362]
- (31). Zhelev Z; Bakalova R; Aoki I; Matsumoto K.-i.; Gadjeva V; Anzai K; Kanno I Nitroxyl Radicals as Low Toxic Spin-Labels for Non-Invasive Magnetic Resonance Imaging of Blood-Brain Barrier Permeability for Conventional Therapeutics. *Chem. Commun* 2009, 53–55.
- (32). Hyodo F; Chuang KH; Goloshevsky AG; Sulima A; Griffiths GL; Mitchell JB; Koretsky AP; Krishna MC Brain Redox Imaging Using Blood-Brain Barrier-Permeable Nitroxide MRI Contrast Agent. *J. Cereb. Blood Flow Metab* 2008, 28, 1165–1174. [PubMed: 18270519]

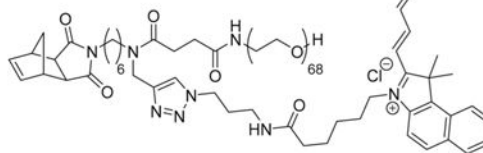
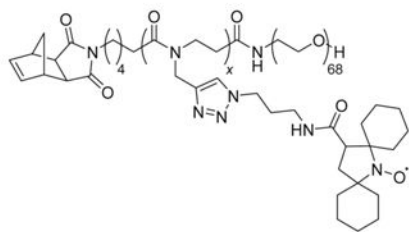
- (33). Brasch RC Work in Progress: Methods of Contrast Enhancement for NMR Imaging and Potential Applications. A Subject Review. *Radiology* 1983, 147, 781–788. [PubMed: 6342034]
- (34). Brasch RC; London DA; Wesbey GE; Tozer TN; Nitecki DE; Williams RD; Doemeny J; Tuck LD; Lallemand DP Work in Progress: Nuclear Magnetic Resonance Study of a Paramagnetic Nitroxide Contrast Agent for Enhancement of Renal Structures in Experimental Animals. *Radiology* 1983, 147, 773–779. [PubMed: 6844613]
- (35). DeVience SJ; Pham LM; Lovchinsky I; Sushkov AO; Bar-Gill N; Belthangady C; Casola F; Corbett M; Zhang H; Lukin M; Park H; Yacoby A; Walsworth RL Nanoscale NMR Spectroscopy and Imaging of Multiple Nuclear Species. *Nat. Nanotechnol* 2015, 10, 129–134. [PubMed: 25559712]
- (36). Preslar AT; Tantakitti F; Park KE; Zhang S; Stupp S; Meade TJ 19F-Magnetic Resonance Imaging Signals from Peptide Amphiphile Nanostructures are Strongly Affected by Their Shape. *ACS Nano* 2016, 10, 7376–7384. [PubMed: 27425636]
- (37). Schmidt AB; Berner S; Schimpf W; Muller C; Lickert T; Schwaderlapp N; Knecht S; Skinner JG; Dost A; Rovedo P; Hennig J; von Elverfeldt D; Hovener JB Liquid-State Carbon-13 Hyperpolarization Generated in an MRI System for Fast Imaging. *Nat. Commun* 2017, 8, 14535. [PubMed: 28262691]
- (38). Duwel S; Hundshammer C; Gersch M; Feuerecker B; Steiger K; Buck A; Walch A; Haase A; Glaser SJ; Schwaiger M; Schilling F Imaging of pH In Vivo Using Hyperpolarized 13C-Labelled Zymonic Acid. *Nat. Commun* 2017, 8, 15126. [PubMed: 28492229]
- (39). Cai K; Haris M; Singh A; Kogan F; Greenberg JH; Hariharan H; Detre JA; Reddy R Magnetic Resonance Imaging of Glutamate. *Nat. Med* 2012, 18, 302–306. [PubMed: 22270722]
- (40). Song X; Airan RD; Arifin DR; Bar-Shir A; Kadayakkara DK; Liu G; Gilad AA; van Zijl PC; McMahon MT; Bulte JW Label-Free In Vivo Molecular Imaging of Underglycosylated Mucin-1 Expression in Tumour Cells. *Nat. Commun* 2015, 6, 6719. [PubMed: 25813863]
- (41). Hyodo F; Soule BP; Matsumoto K.-i.; Matusmoto S; Cook JA; Hyodo E; Sowers AL; Krishna MC; Mitchell JB Assessment of Tissue Redox Status Using Metabolic Responsive Contrast Agents and Magnetic Resonance Imaging. *J. Pharm. Pharmacol* 2008, 60, 1049–1060. [PubMed: 18644197]
- (42). Hyodo F; Matsumoto K.-i.; Matsumoto A; Mitchell JB; Krishna MC Probing the Intracellular Redox Status of Tumors with Magnetic Resonance Imaging and Redox-Sensitive Contrast Agents. *Cancer Res* 2006, 66, 9921–9928. [PubMed: 17047054]
- (43). Zhelev Z; Bakalova R; Aoki I; Matsumoto K.-i.; Gadjeva V; Anzai K; Kanno I Nitroxyl Radicals for Labeling of Conventional Therapeutics and Noninvasive Magnetic Resonance Imaging of Their Permeability for Blood–Brain Barrier: Relationship between Structure, Blood Clearance, and MRI Signal Dynamic in the Brain. *Mol. Pharmaceutics* 2009, 6, 504–512.
- (44). Zhelev Z; Bakalova R; Aoki I; Lazarova D; Saga T Imaging of Superoxide Generation in the Dopaminergic Area of the Brain in Parkinson’s Disease, Using Mito-TEMPO. *ACS Chem. Neurosci* 2013, 4, 1439–1445. [PubMed: 24024751]
- (45). Rajca A; Wang Y; Boska M; Paletta JT; Olankitwanit A; Swanson MA; Mitchell DG; Eaton SS; Eaton GR; Rajca S Organic Radical Contrast Agents for Magnetic Resonance Imaging. *J. Am. Chem. Soc* 2012, 134, 15724–15727. [PubMed: 22974177]
- (46). Rajca A; Wang Y; Boska M; Paletta JT; Olankitwanit A; Swanson MA; Mitchell DG; Eaton SS; Eaton GR; Rajca S Correction to Organic Radical Contrast Agents for Magnetic Resonance Imaging. *J. Am. Chem. Soc* 2014, 136, 3318–3318. [PubMed: 24533533]
- (47). Sowers MA; McCombs JR; Wang Y; Paletta JT; Morton SW; Dreaden EC; Boska MD; Ottaviani MF; Hammond PT; Rajca A; Johnson JA Redox-Responsive Branched-Bottlebrush Polymers for In Vivo MRI and Fluorescence Imaging. *Nat. Commun* 2014, 5, 5460. [PubMed: 25403521]
- (48). Nguyen HV; Chen Q; Paletta JT; Harvey P; Jiang Y; Zhang H; Boska MD; Ottaviani MF; Jasanoff A; Rajca A; Johnson JA Nitroxide-Based Macromolecular Contrast Agents with Unprecedented Transverse Relaxivity and Stability for Magnetic Resonance Imaging of Tumors. *ACS Cent. Sci* 2017, 3, 800–811. [PubMed: 28776023]
- (49). Hansen K-A; Blinco JP Nitroxide Radical Polymers – a Versatile Material Class for High-Tech Applications. *Polym. Chem* 2018, 9, 1479–1516.

- (50). Cagliaris F; Melone L; Canepa F; Lamura G; Castiglione F; Ferro M; Malpezzi L; Mele A; Punta C; Franchi P; Lucarini M; Rossi B; Trotta F Effective Magnetic Moment in Cyclodextrin–Polynitroxides: Potential Supramolecular Vectors for Magnetic Resonance Imaging. *RSC Adv* 2015, 5, 76133–76140.
- (51). Bye N; Hutt OE; Hinton TM; Acharya DP; Waddington LJ; Moffat BA; Wright DK; Wang HX; Mulet X; Muir BW Nitroxide-Loaded Hexosomes Provide MRI Contrast In Vivo. *Langmuir* 2014, 30, 8898–8906. [PubMed: 24979524]
- (52). Chan JMW; Wojtecki RJ; Sardon H; Lee ALZ; Smith CE; Shkumatov A; Gao S; Kong H; Yang YY; Hedrick JL Self-Assembled, Biodegradable Magnetic Resonance Imaging Agents: Organic Radical-Functionalized Diblock Copolymers. *ACS Macro Lett* 2017, 6, 176–180.
- (53). Huang Y; Nan A; Rosen GM; Winalski CS; Schneider E; Tsai P; Ghandehari H N-(2-Hydroxypropyl)methacrylamide (HPMA) Copolymer-Linked Nitroxides: Potential Magnetic Resonance Contrast Agents. *Macromol. Biosci* 2003, 3, 647–652.
- (54). Gussoni M; Greco F; Ferruti P; Ranucci E; Ponti A; Zetta L Poly(amidoamine)s Carrying TEMPO Residues for NMR Imaging Applications. *New J. Chem* 2008, 32, 323–332.
- (55). Garmendia S; Mantione D; Alonso-de Castro S; Jehanno C; Lezama L; Hedrick JL; Mecerreyes D; Salassa L; Sardon H Polyurethane Based Organic Macromolecular Contrast Agents (PU-ORCAs) for Magnetic Resonance Imaging. *Polym. Chem* 2017, 8, 2693–2701.
- (56). Huang L; Yan C; Cui D; Yan Y; Liu X; Lu X; Tan X; Lu X; Xu J; Xu Y; Liu R Organic Radical Contrast Agents Based on Polyacetylenes Containing 2,2,6,6-Tetramethylpiperidine 1-Oxyl (TEMPO): Targeted Magnetic Resonance (MR)/Optical Bimodal Imaging of Folate Receptor Expressing HeLa Tumors In Vitro and In Vivo. *Macromol. Biosci* 2015, 15, 788–798. [PubMed: 25677802]
- (57). Liu J; Burts AO; Li Y; Zhukhovitskiy AV; Ottaviani MF; Turro NJ; Johnson JA Brush-First” Method for the Parallel Synthesis of Photocleavable, Nitroxide-Labeled Poly(Ethylene Glycol) Star Polymers. *J. Am. Chem. Soc* 2012, 134, 16337–16344. [PubMed: 22953714]
- (58). Liao L; Liu J; Dreaden EC; Morton SW; Shopsowitz KE; Hammond PT; Johnson JA A Convergent Synthetic Platform for Single-Nanoparticle Combination Cancer Therapy: Ratiometric Loading and Controlled Release of Cisplatin, Doxorubicin, and Camptothecin. *J. Am. Chem. Soc* 2014, 136, 5896–5899. [PubMed: 24724706]
- (59). Gao AX; Liao L; Johnson JA Synthesis of Acid-Labile PEG and PEG-Doxorubicin-Conjugate Nanoparticles via Brush-First ROMP. *ACS Macro Lett* 2014, 3, 854–857. [PubMed: 25243099]
- (60). Barnes JC; Bruno PM; Nguyen HVT; Liao L; Liu J; Hemann MT; Johnson JA Using an RNAi Signature Assay To Guide the Design of Three-Drug-Conjugated Nanoparticles with Validated Mechanisms, In Vivo Efficacy, and Low Toxicity. *J. Am. Chem. Soc* 2016, 138, 12494–12501. [PubMed: 27626288]
- (61). Golder MR; Liu J; Andersen JN; Shipitsin MV; Vohidov F; Nguyen HV-T; Ehrlich DC; Huh SJ; Vangamudi B; Economides KD; Neenan AM; Ackley JC; Baddour J; Paramasivan S; Brady SW; Held EJ; Reiter LA; Saucier-Sawyer JK; Kopesky PW; Chickering DE; et al. Reduction of Liver Fibrosis by Rationally Designed Macromolecular Telmisartan Prodrugs. *Nat. Biomed. Eng* 2018, 2, 707.
- (62). Cabral H; Matsumoto Y; Mizuno K; Chen Q; Murakami M; Kimura M; Terada Y; Kano MR; Miyazono K; Uesaka M; Nishiyama N; Kataoka K Accumulation of Sub-100 nm Polymeric Micelles in Poorly Permeable Tumours Depends on Size. *Nat. Nanotechnol* 2011, 6, 815–823. [PubMed: 22020122]
- (63). Elsbahy M; Heo GS; Lim S-M; Sun G; Wooley KL Polymeric Nanostructures for Imaging and Therapy. *Chem. Rev* 2015, 115, 10967–11011. [PubMed: 26463640]
- (64). Nguyen HVT; Gallagher NM; Vohidov F; Jiang Y; Kawamoto K; Zhang H; Park JV; Huang Z; Ottaviani MF; Rajca A; Johnson JA Scalable Synthesis of Multivalent Macro-monomers for ROMP. *ACS Macro Lett* 2018, 7, 472–476. [PubMed: 30271675]
- (65). Cheon J; Lee J-H Synergistically Integrated Nanoparticles as Multimodal Probes for Nanobiotechnology. *Acc. Chem. Res* 2008, 41, 1630–1640. [PubMed: 18698851]
- (66). Jokerst JV; Lobovkina T; Zare RN; Gambhir SS Nanoparticle PEGylation for Imaging and Therapy. *Nanomedicine* 2011, 6, 715–728. [PubMed: 21718180]

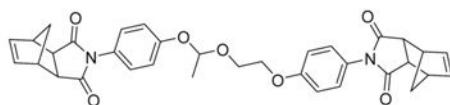
- (67). Maeda H; Wu J; Sawa T; Matsumura Y; Hori K Tumor Vascular Permeability and the EPR Effect in Macromolecular Therapeutics: A Review. *J. Controlled Release* 2000, 65, 271–284.
- (68). Keana JFW; Pou S; Rosen GM Nitroxides as Potential Contrast Enhancing Agents for MRI Application: Influence of Structure on the Rate of Reduction by Rat Hepatocytes, Whole Liver Homogenate, Subcellular Fractions, and Ascorbate. *Magn. Reson. Med* 1987, 5, 525–536. [PubMed: 3437813]
- (69). Yang Y; Zhao Q; Feng W; Li F Luminescent Chemo-dosimeters for Bioimaging. *Chem. Rev* 2013, 113, 192–270. [PubMed: 22702347]
- (70). Rowland M; Benet LZ; Graham GG Clearance Concepts in Pharmacokinetics. *J. Pharmacokinet. Biopharm* 1973, 1, 123–136. [PubMed: 4764426]
- (71). Qi R; Wang Y; Bruno PM; Xiao H; Yingjie Y; Li T; Lauffer S; Wei W; Chen Q; Kang X; Song H; Yang X; Huang X; Detappe A; Matulonis U; Pepin D; Hemann MT; Birrer MJ; Ghoroghchian PP Nanoparticle Conjugates of a Highly Potent Toxin Enhance Safety and Circumvent Platinum Resistance in Ovarian Cancer. *Nat. Commun* 2017, 8, 2166. [PubMed: 29255160]
- (72). Rajkumar SV; Dimopoulos MA; Palumbo A; Blade J; Merlini G; Mateos MV; Kumar S; Hillengass J; Kastritis E; Richardson P; Landgren O; Paiva B; Dispenzieri A; Weiss B; LeLeu X; Zweegman S; Lonial S; Rosinol L; Zamagni E; Jagannath S; et al. International Myeloma Working Group Updated Criteria for the Diagnosis of Multiple Myeloma. *Lancet Oncol* 2014, 15, 538–548.
- (73). Ji Y; Jiang C; Zhang X; Liu W; Gao M; Li Y; Wang J; Wang Q; Sun Z; Jiang X; Yao N; Wang X; Fang Z; Yin Z; Ni Y; Zhang J Necrosis Targeted Combinational Theragnostic Approach Using Radiiodinated Sennidin A in Rodent Tumor Models. *Oncotarget* 2014, 5, 2934–2946. [PubMed: 24931286]
- (74). Rey S; Schito L; Koritzinsky M; Wouters BG Molecular Targeting of Hypoxia in Radiotherapy. *Adv. Drug Delivery Rev* 2017, 109, 45–62.
- (75). Xiao H; Qi R; Li T; Awuah SG; Zheng Y; Wei W; Kang X; Song H; Wang Y; Yu Y; Bird MA; Jing X; Yaffe MB; Birrer MJ; Ghoroghchian PP Maximizing Synergistic Activity When Combining RNAi and Platinum-Based Anticancer Agents. *J. Am. Chem. Soc* 2017, 139, 3033–3044. [PubMed: 28166401]
- (76). Tao Z; Dang X; Huang X; Muzumdar MD; Xu ES; Bardhan NM; Song H; Qi R; Yu Y; Li T; Wei W; Wyckoff J; Birrer MJ; Belcher AM; Ghoroghchian PP Early Tumor Detection Afforded by In Vivo Imaging of Near-Infrared II Fluorescence. *Biomaterials* 2017, 134, 202–215. [PubMed: 28482280]
- (77). Burts AO; Liao L; Lu YY; Tirrell DA; Johnson JA Brush-First and Click: Efficient Synthesis of Nanoparticles that Degrade and Release Doxorubicin in Response to Light. *Photochem. Photobiol* 2014, 90, 380–385. [PubMed: 24117423]
- (78). Johnson JA; Lu YY; Burts AO; Xia Y; Durrell AC; Tirrell DA; Grubbs RH Drug-Loaded, Bivalent-Bottle-Brush Polymers by Graft-through ROMP. *Macromolecules* 2010, 43, 10326–10335. [PubMed: 21532937]

A Compounds used for BASP-ORCA synthesis:

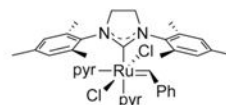
branched macromonomers:



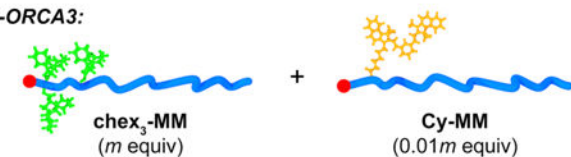
crosslinker:  **Acetal-XL**




initiator: **Grubbs III**



B Synthesis of BASP-ORCA3:



1) Grubbs III (1 equiv)
tetrahydrofuran, 30 min, RT

2) **Acetal-XL** (N equiv) 
6 h, RT

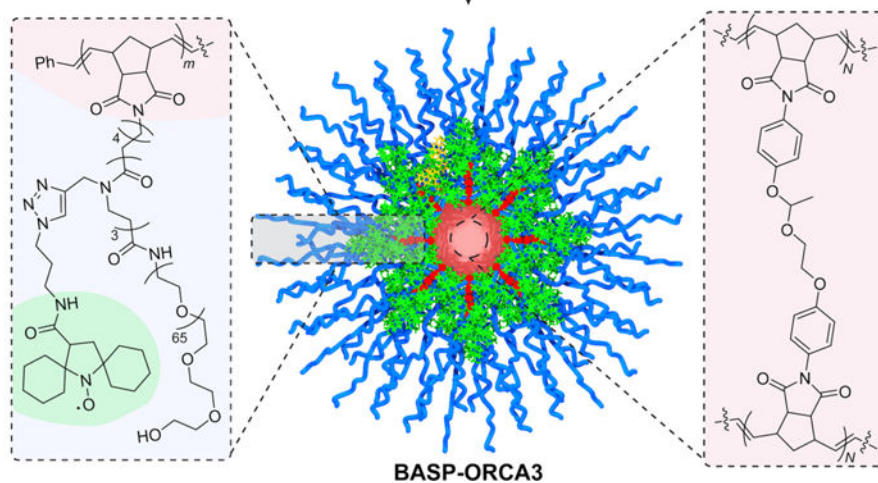


Figure 1.

Chemical structures and scheme for the synthesis of BASP-ORCAs. (A) Structures of BASP-ORCA components used in this work and (B) brush-first ring-opening metathesis polymerization (ROMP) scheme for the preparation of BASP-ORCA3 pyr = pyridine; Ph = phenyl.

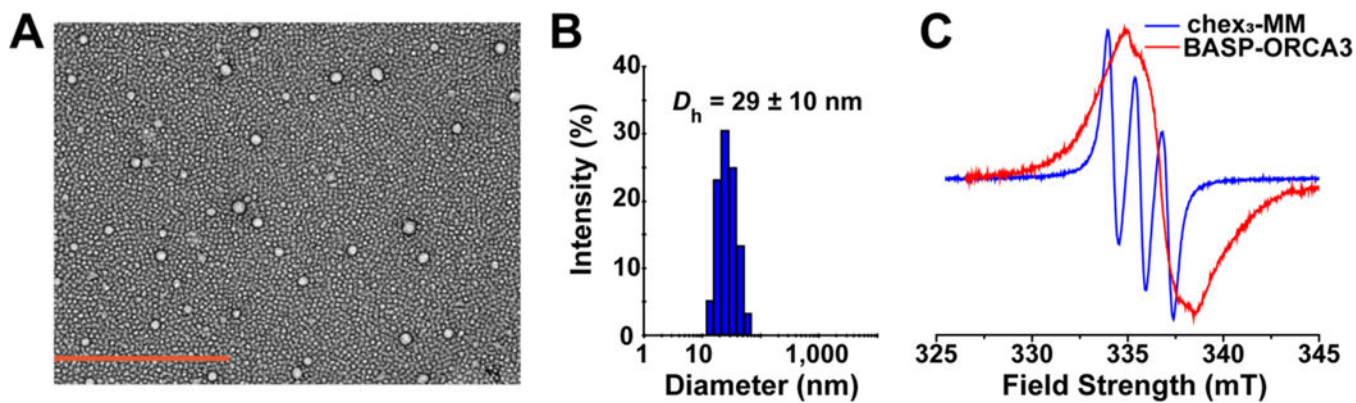


Figure 2.

In vitro characterization of BASP-ORCA3. (A) Representative transmission electron microscopy (TEM) image of BASP-ORCA3 (negatively stained with 2% wt. uranyl acetate). Scale bar: 500 nm. (B) Representative dynamic light scattering (DLS) histogram for BASP-ORCA3. D_h = hydrodynamic diameter. (C) Electron paramagnetic resonance (EPR) spectra for BASP-ORCA3 and cheX₃-MM.

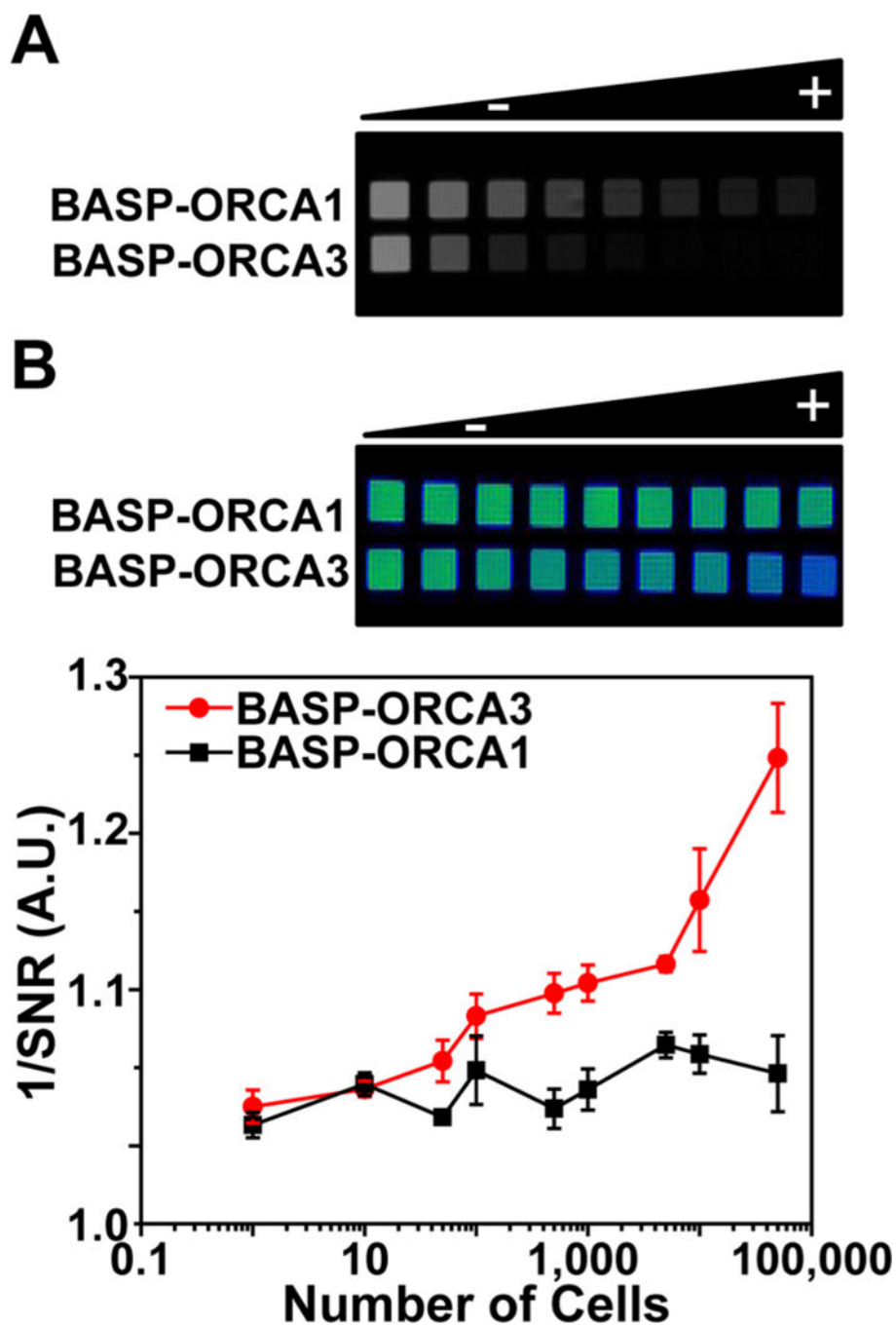


Figure 3. MRI phantoms of BASP-ORCA3. (A) T_2 -weighted MRI phantoms at the same w/v concentrations (from 0 to 3, 6, 8, 12, 15, 18, and 21 mg/mL) of BASP-ORCA1 and BASP-ORCA3, which vary by chex density. (B) T_2 -weighted MRI phantoms (top) and quantification of *in vitro* sensitivity (bottom) of BASP-ORCA1 and BASP-ORCA3 at 6 h after incubation with MM.1S cells with 21 mg/mL BASP-ORCA solutions.

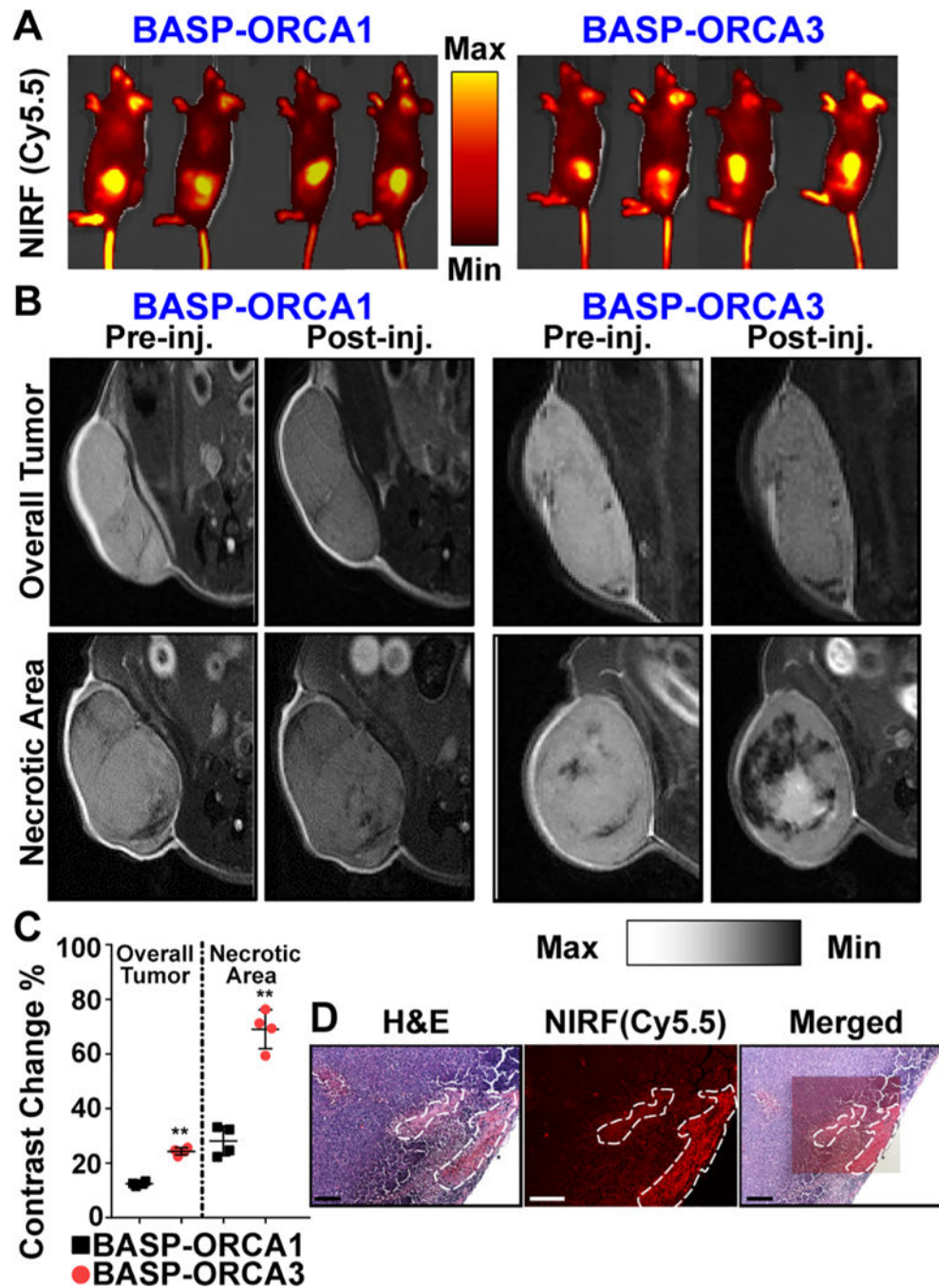


Figure 4. *In vivo* imaging of subcutaneous plasmacytomas. (A) *In vivo* optical imaging (Cy5.5 fluorescence; $\lambda_{ex}/\lambda_{em} = 640/700$ nm) of MM.1S (multiple myeloma) cells subcutaneously implanted in SCID mice ($n = 4$); the animals were administered either BASP-ORCA1 or BASP-ORCA3 by intravenous injection and their tumors were visualized 24 h later by *in vivo* optical imaging. (B) T_2 -weighted MR images of the same mice pre- and postinjection, revealing differences in T_2 signal observed from BASP-ORCA1 vs BASP-ORCA3 and in both non-necrotic and necrotic tumor regions. (C) Quantitative analysis of contrast

enhancements generated by BASP-ORCA1 vs BASP-ORCA3 in the overall tumor versus in necrotic regions. Statistical comparisons were acquired with the Mann–Whitney U -test (*not significant, ** $p < 0.05$, *** $p < 0.01$). (D) Colocalization study confirming the specific uptake of BASP-ORCA3 (based on its Cy5.5 signal) in necrotic tumor areas as depicted by H&E staining.

Author Manuscript

Author Manuscript

Author Manuscript

Author Manuscript

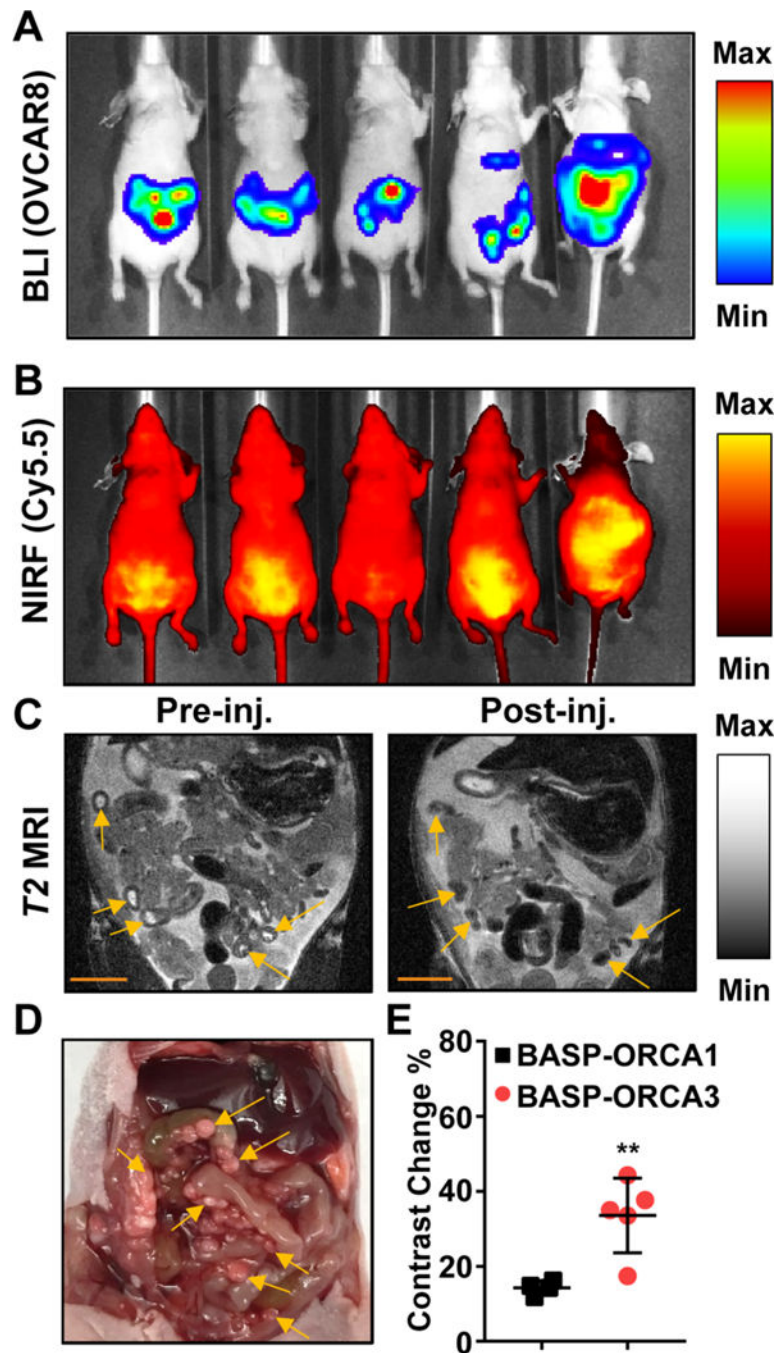


Figure 5. *In vivo* detection of millimetric tumor deposits in a murine model of disseminated ovarian cancer. (A) Growth of luciferase-expressing OVCAR8 (ovarian) tumors monitored by bioluminescence imaging (BLI). (B) Tumor accumulation of BASP-ORCA3 qualitatively visualized by *in vivo* optical imaging of its near-infrared fluorescence at 24 h after intraperitoneal injection. (C) T_2 -weighted MR images of the same mice pre- and postinjection with BASP-ORCA3, demonstrating millimetric tumors on the serosal surfaces of peritoneal organs (yellow arrows). Scale bar: 1 cm. (D) Visual validation of tumor

implants (yellow arrows). (E) Quantitative analysis of contrast enhancement generated by BASP-ORCA1 vs BASP-ORCA3. Statistical comparisons were acquired with the Mann–Whitney *U*-test (*not significant, ** $p < 0.05$, *** $p < 0.01$).

Author Manuscript

Author Manuscript

Author Manuscript

Author Manuscript

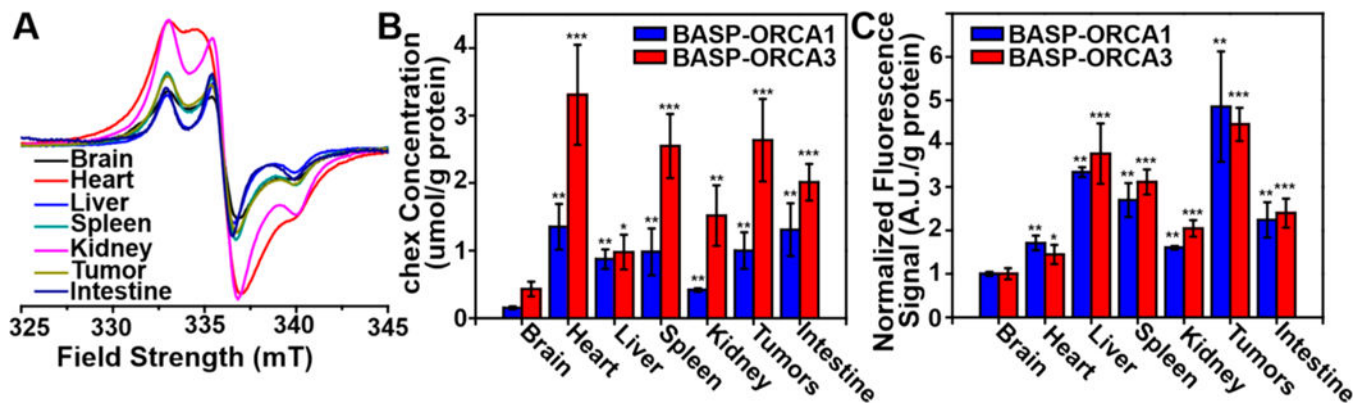


Figure 6. Quantification of the biodistribution profiles of different BASP-ORCAs via quantification of EPR and fluorescence signals in *ex vivo* organ homogenates from the OVCAR8 (ovarian tumor) model. (A) Representative EPR spectra of *ex vivo* organ homogenates from mice administered BASP-ORCA3. (B) Quantification of chex content in each organ by EPR ($n = 4-5$), revealing greater amounts of chex across the various organs of mice that were administered BASP-ORCA3 vs BASP-ORCA1. (C) Biodistribution profiles as quantified from NIRF signals, revealing similar profiles for BASP-ORCA1 and BASP-ORCA3; the results support that the higher tumor contrast imparted by BASP-ORCA3 is due to its increased chex loading. Statistical comparisons between sample tissues and brain tissue were acquired using the Mann–Whitney U -test (*not significant, ** $p < 0.05$, *** $p < 0.01$).